Particuology 115 (2026) 356–365

Contents lists available at ScienceDirect

Particuology

journal homepage: www.elsevier.com/locate/partic

Settling dynamics of micro-sized char and coal powders: An experimental study

Wenyu Tu[a,1], Peilin Tian[a,1], Liang-Liang Fan[b,*], Liang Zhao[a,**]

[a] *State Key Laboratory of Multiphase Flow in Power Engineering, Xi'an Jiaotong University, Xi'an, 710049, China*
[b] *School of Instrument Science and Technology, Xi'an Jiaotong University, Xi'an, 710049, China*

HIGHLIGHTS

- Drag coefficients for char particles are derived for the first time.
- Stokes and Schiller drag formulations are revised for coal and char particles.
- Rough char surfaces from pyrolysis yield higher drag coefficients.
- The model modified by this work refines char pneumatic conveying simulations.

GRAPHICAL ABSTRACT

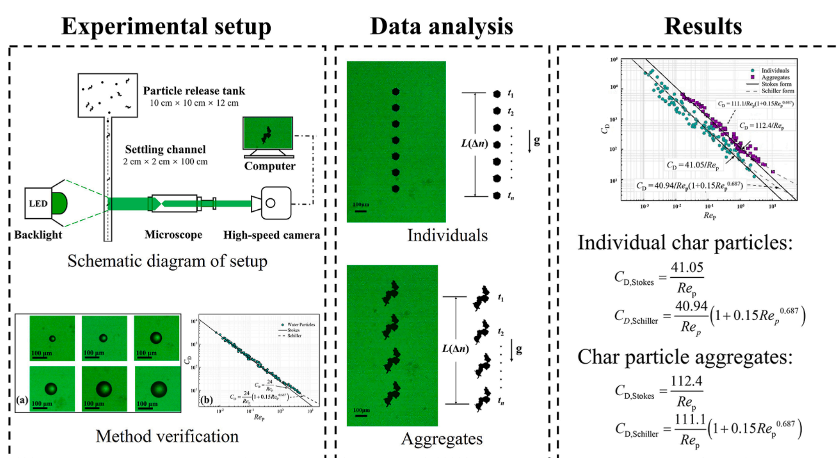

ARTICLE INFO

Keywords:
Settling dynamics
Char powder
Coal powder
Drag coefficient
Settling velocity

ABSTRACT

Char particles from coal pyrolysis exhibit unique settling dynamics, such as terminal velocity and drag coefficient. Accurate quantification of drag characteristics is essential for pneumatic conveying. Current simulations adopting spherical drag models suffer large deviations for irregular char particles. To fill this gap, we built a visual platform to investigate free settling of coal and char particles (<200 μm). Terminal velocities were measured for individual particles and aggregates. Based on statistical analysis, we revised Stokes and Schiller drag formulations. In the Stokes form, the fitted coefficients for individual coal particles and coal aggregates are 26.04 ± 3.5 and 52.15 ± 4.8, respectively; for individual char particles and char aggregates, they are 41.05 ± 3.2 and 112.4 ± 4.3, respectively. In the Schiller form, the fitted coefficients for individual coal particles and coal aggregates are 26.19 ± 3.4 and 53.88 ± 4.2, respectively; for individual char particles and char aggregates, they are 40.94 ± 3.2 and 111.1 ± 4.2, respectively. These correlations can be directly employed in drag model for numerical simulation of char pneumatic conveying. Validation shows significantly improved accuracy. This work

* Corresponding author.
** Corresponding author.
E-mail addresses: fanllxj@xjtu.edu.cn (L.-L. Fan), lzhao@mail.xjtu.edu.cn (L. Zhao).
[1] These authors contributed equally to this work.

https://doi.org/10.1016/j.partic.2026.05.022
Received 3 February 2026; Received in revised form 17 May 2026; Accepted 29 May 2026
Available online 6 June 2026

presents the first experimentally derived drag coefficient correlations for char particles, addressing the lack of quantitative data and offering a more precise tool for char transport design.

Nomenclature

a	Fitted coefficient in drag coefficient correlations	G	Gravitational force of the particle (N)
A_f	Reference area of the particle (μm^2)	g	Gravitational acceleration (m s^{-2})
A_{sh}	Two-dimensional projected area of the particle on the imaging plane (μm^2)	L (Δn)	Settling displacement of the particle over a duration of n frames (m)
C_D	Drag coefficient	Re_p	Particle Reynolds number
d_{eq}	Equivalent particle diameter based on projected area (μm)	U_t	Terminal settling velocity of the particle (m s^{-1})
d_p	Particle diameter (μm)	u_g	Gas velocity (m s^{-1})
D_{50}	Particle diameter at 50% cumulative percentage of the particle size distribution (μm)	μ	Dynamic viscosity of the fluid (Pa s)
f	Frame rate of the high-speed camera (s^{-1})	ρ_f	Density of the fluid (kg m^{-3})
F_B	Buoyant force acting on the particle (N)	ρ_p	Density of the particle (kg m^{-3})
F_D	Drag force acting on the particle (N)		

1. Introduction

With the increasing global energy demand, the full utilization of char powder is of significant importance for improving energy efficiency. During the utilization process, char powder is often transported pneumatically, for example, in industrial processes, it is typically injected into gasifiers, metallurgical furnaces, and combustion boilers via pneumatic conveying (Cai et al., 2023; Tang et al., 2017; Xiao et al., 2024; Zhu et al., 2022). The settling dynamics of micron-sized char powder particles play a crucial role in the efficiency and safety of pneumatic conveying. The pneumatic conveying behavior of char powder particles depends on the interaction forces between the particles and the carrier gas. These forces typically include drag force, thermophoretic force, Brownian force, added mass force, pressure-gradient force, history force, and lift force (Marshall & Li, 2014). Existing studies have shown that among these forces, the drag force is the dominant factor influencing the dynamic behavior of particles (Marshall & Li, 2014). The accuracy of the drag coefficient is essential for determining the magnitude of the drag force acting on the particles. In current research on pneumatic conveying simulations, Euler-Lagrange and Euler-Euler schemes are commonly employed. In these methods, the drag coefficient for spherical particles is often used to model the momentum exchange between the gas and solid phase (Li & Tomita, 2000; Ma et al., 2012; Miao et al., 2020; Pu et al., 2010). However, char powder particles, as a product of coal pyrolysis, exhibit irregular shapes and porous structural characteristics. Applying the drag coefficient of spherical particles to study the behavior of char particles will lead to significant deviations. Therefore, it is necessary to investigate the dynamic behavior of non-spherical char powder particles to determine an accurate drag coefficient.

Currently, extensive research has been conducted in academia on the drag coefficient of spherical particles, and numerous high-precision drag coefficient correlations have been derived through theoretical and experimental studies on the free settling process of spherical particles. This is because for regular spherical particles, the drag coefficient is solely a function of the particle Reynolds number, and the influence of particle shape on the results is not involved, making variable control relatively straightforward (Brown & Lawler, 2003; Clift & Gauvin, 1971; Goossens, 2019; Loth, 2008; Song et al., 2008). Nevertheless, the applicability of such correlations diminishes for non-spherical particles, as the drag coefficient in this condition depends not only on the particle Reynolds number but also critically on the particle morphology. Non-spherical particles can be divided into regularly shaped particles (e.g., ellipsoids, cylinders, disks) and irregularly shaped particles (non-symmetric rough surfaces). Loth (2008) and Marchildon et al. (1964) studied the drag coefficients of regularly shaped non-spherical particles, using the aspect ratio to characterize the morphological features of various particle types such as octahedra, tetrahedra, and sphere clusters, thereby establishing drag coefficient correlations for these regular non-spherical particles. The aspect ratio is defined as the ratio between the parallel and normal diameters; it is a two-dimensional morphological parameter that can be easily obtained from microscope images, but its applicability is poor for particles with high non-sphericity. The concept of sphericity helps to understand the degree of similarity between the shape of a non-spherical particle and that of a spherical particle. Sphericity is defined as the ratio of the surface area of a spherical particle with the same volume as the given particle to the surface area of the given particle. Hussain and Munshi (2024), Haider and Levenspiel (1989), Ganser (1993), and Hölzer and Sommerfeld (2008) used sphericity to characterize the shape factor of smooth-surfaced and regularly shaped non-spherical particles, expressing the drag coefficient of these particles as a function of particle Reynolds number and sphericity, thus establishing high-accuracy drag coefficient correlations for non-spherical particles.

Another category of non-spherical particles is comprised of those with non-symmetric rough surfaces, such as natural sands and volcanic ash, for which the study of drag coefficients poses greater challenges in describing their morphology. Coarse ore particles are a typical example of highly irregular particles. Xu et al. (2024) proposed that although coarse ore particles differ from spherical particles in settling dynamics, they follow similar motion laws; therefore, by introducing the equivalent particle diameter of irregular coarse ore particles into the empirical formula for spherical particles for correction, the applicability of the prediction formula for spherical particles was extended to enable the prediction of drag coefficient for coarse particles. On the basis of the five-parameter drag model by Cheng (2009), a drag coefficient correlation for coarse particles was fitted. Fang et al. (2021) conducted particle settling experiments using four types of highly irregular micron-sized graphite particles and employed different equivalent diameter characterization methods for particles of different morphologies: the volume-equivalent diameter for single particles and the projected-area-equivalent diameter for particle aggregates. The study found that within the Stokes regime, despite the high degree of particle irregularity, the drag coefficient still followed an inverse relationship with the Reynolds number. Empirical coefficients for the four different graphite particles were fitted, and over a wider range of particle Reynolds numbers, the experimental results agreed well with the correlations of Bagheri and Bonadonna (2016, 2019). Ma et al. (2022) established a baseline model through experiments with spherical particles and introduced the easily measurable two-dimensional shape parameter circularity as a correction factor to modify the drag coefficient calculation formula for spherical particles, thereby constructing a modified drag coefficient model for natural quartz sand. Thanks to the easy accessibility of two-dimensional parameters, this method significantly improved model applicability; however, relying solely on circularity as a single parameter could not fully capture the influence of complex shapes, and prediction deviations remained relatively high.

To more accurately characterize the effect of the complex morphology of highly irregular coarse particles on settling dynamics, Wang et al. (2018) and Dioguardi and Mele (2015) adopted a new shape descriptor: the ratio of sphericity to inverse circularity, as a shape parameter for coarse particles. Using highly irregular calcareous sand particles and volcanic ash as experimental materials, they established modified drag coefficient models for highly irregular coarse particles within the ranges of $Re < 10^3$ and $5 < Re < 1000$, respectively. Dioguardi et al. (2018) proposed a novel single-equation drag correction model based on hundreds of settling data points of volcanic ash and lapilli particles. The study found that the new model not only eliminates the jump discontinuity of the original model at the critical Reynolds number, ensuring continuity over the entire calculation range, but also perfectly degenerates into the standard spherical particle drag curve when the shape factor approaches 1. This model exhibits significantly improved prediction accuracy at extremely low Reynolds numbers, providing a more robust computational tool for numerical simulations of multiphase flows. Liu et al. (2024) proposed a novel coupled shape factor characterization method for the problem of irregular particle plume dispersion caused by deep-sea mining. This method comprehensively considers the one-dimensional, two-dimensional, and three-dimensional geometric characteristics of irregular particles and their coupling effects, and establishes a modified drag coefficient model for irregular particles. The study confirmed that this modified model has higher computational accuracy and applicability than existing classical models over an extremely wide Reynolds number range ($Re < 3 \times 10^5$). Widely used drag coefficient correlations for both regular and irregular particles are summarized in Table 1.

Research on the drag coefficient of non-spherical particles has revealed that variations in shape, morphology, and structure lead to distinct drag coefficients among different types of non-spherical particles. Consequently, individualized studies are required for specific particle types. Char powder is a special material derived from pulverized coal pyrolysis and serves as an important intermediate product in the low-rank coal grading utilization process. Its settling dynamics are of significant research importance and have broad industrial application prospects, such as in pneumatic conveying, furnace injection, and dust pollution control of char powder. However, it is noted that publicly available studies on the settling dynamics of char particles derived from pulverized coal pyrolysis are lacking. It is therefore necessary to investigate the settling dynamics of char powder particles to obtain their accurate drag coefficient.

In order to accurately determine the drag coefficient of char particle in air, an experimental system for visualizing the free-settling behavior of particles was established in this study. The settling dynamics of parent coal particles and their derived char particles with diameters below 200 μm were investigated experimentally. Terminal settling velocities and corresponding drag coefficients were individually determined for individual char particles, char aggregates, individual coal particles, and coal aggregates. Furthermore, the microscopic morphology characteristics of both coal and char were characterized via scanning electron microscopy. Extensive statistical analysis was conducted on a large population of particles, and the obtained drag coefficients were modeled using both Stokes and the Schiller formulations. The developed model demonstrates reliable applicability across a wide range of particle Reynolds numbers.

Table 1
Widely used correlations of the drag coefficient of both regular and irregular particles.

Proposer refs.	Correlations	Applications
Stokes (2009)	$C_D = \frac{24}{Re_p}$	$Re_p < 1$ Smooth spheres
Schiller and Naumann (1933)	$C_D = \frac{24}{Re_p}(1 + 0.15Re_p^{0.687})$	$Re_p < 800$ Smooth spheres
Clift and Gauvin (1971)	$C_D = \frac{24}{Re_p}(1 + 0.15Re_p^{0.687}) + \frac{0.42}{1 + \frac{42500}{Re_p^{1.16}}}$	$Re_p < 3 \times 10^5$ Smooth spheres
Brown and Lawler (2003)	$C_D = \frac{24}{Re}(1 + 0.15Re^{0.681}) + \frac{0.407}{1 + 8710Re^{-1}}$	$Re_p < 2 \times 10^5$ Spheres
Song et al. (2017)	$C_D = \frac{24}{Re_n(\phi^{0.65}S^{0.3})}(1 + 0.35Re_n)^{0.44}$ $S = \frac{S_e}{S_p}$	$Re_p < 100$ $0.471 < \phi < 1$ Regular particles
Hussain and Munshi (2024)	$C_{D\infty} = \frac{22}{Re_\infty}(1 + 0.19Re^{0.46\psi})$ $C_D = \frac{2.16}{Re}\left(1 + 0.12Re^{1.16\psi} + 17.6\left(\frac{d_{eq}}{L}\right)^{0.0613}\right)$	Disk particle and cylinder particle
Ma et al. (2022)	$C_D = C_{D,sph}\exp\left[1.45{Re_s}^{0.07}(1 - c)^{0.13}\right]$ $c = \frac{4\pi A_p}{{P_p}^2}$	$0.02 < Re_p < 1130$ Natural quartz sand
Liu et al. (2024)	$C_D = \frac{24}{Re} \cdot f_1(\gamma) + \frac{24}{Re}(0.15Re^{0.687}) \cdot f_1(\gamma) + \frac{0.42}{1 + \frac{42500}{Re^{1.16}} \cdot f_1(\gamma)}$ $f_1(\gamma) = \gamma^{-0.0035A^{1.95}}$ $f_2(\gamma) = \left(1 + \frac{1 - \gamma}{37 - 1.49A}\right)^{4.75A - 33.8}$ $f_3(\gamma) = 0.11 + 0.89\gamma$ $A = A + \log_{10} Re$	$Re_p < 3 \times 10^5$ Irregular non-spherical particles
Dioguardi and Mele (2015)	$C_D = \frac{C_{d,sphere}}{Re^2\psi^n}\left(\frac{Re}{1.1883}\right)^{1/0.4826}$	$Re_p < 10^4$ Non-spherical rough particles
Dioguardi et al. (2018)	$C_D = \frac{24}{Re}\left(\frac{1 - \psi}{Re} + 1\right)^{0.25} + \frac{24}{Re}(0.1806Re^{0.6459})\psi^{-(Re^{0.08})} + \frac{0.4251}{1 + \frac{6880.95}{Re}\psi^{-5.05}}$	$0.03 < Re_p < 10^4$ Volcanic ash
Wang et al. (2018)	$C_D = 0.945\frac{C_{D,sphere}}{\psi^{exp}}Re_P$ $exp = 0.641Re_P^{0.153}$	Highly irregular calcareous particles
Xu et al. (2024)	$C_D = \frac{24}{Re_s}(1 + 52.02Re_s)^{0.062} - 0.32\left[1 - \exp\left(2.32{Re_s}^{1.47}\right)\right]$	$Re_p < 10^3$ Mineral particles

2. Experimental

2.1. Theoretical basis

When a particle reaches a steady state during free settling, the equilibrium among gravitational force, buoyant force, and the fluid drag force acting on the particle can be established through force balance analysis, as expressed in the following equation:

$$G - F_D - F_B = 0 \tag{1}$$

where G is the gravitational force of the particle, F_D is the drag force of the particle, and F_B is the buoyant force of the particle. For a spherical particle with a diameter of d_p, F_D can be calculated as follows:

$$F_D = \frac{\pi}{6} d_p^3 (\rho_p - \rho_f) g = \frac{1}{2} C_D \rho_f A_f U_t^2 \tag{2}$$

where ρ_p is the particle density, ρ_f is the fluid density, g represents the gravitational acceleration, A_f is a reference area related to the particle size (e.g. $\pi d^2/4$ for a sphere with diameter of d) and U_t is the terminal settling velocity of the particle. Therefore, the drag coefficient C_D can be derived and expressed as follows:

$$C_D = \frac{4 g d_p (\rho_p - \rho_f)}{3 \rho_f U_t^2} \tag{3}$$

The drag coefficient C_D is a dimensionless parameter that can be used to characterize the settling dynamics of the particle, and it is directly correlated with the particle Reynolds number (Re_p) (Fang et al., 2021):

$$Re_p = \frac{\rho_f U_t d_p}{\mu} \tag{4}$$

where μ is the dynamic viscosity of the fluid.

Stokes (Stokes, 2009) gives an analytical solution to the drag coefficient of spherical particles at $Re_p < 0.1$:

$$C_D = \frac{24}{Re_P} \tag{5}$$

Furthermore, the Schiller correlation (Schiller & Naumann, 1933) shows good applicability in a larger range of particle Reynolds numbers, with its expression given as follows:

$$C_D = \frac{24}{Re_P}\left(1 + 0.15 Re_P^{0.687}\right) \quad Re_P < 800 \tag{6}$$

In this study, both Stokes and Schiller expressions will be used to fit the drag coefficients of the coal and the char particles:

$$C_D = \frac{a_{stokes}}{Re_P} \tag{7}$$

$$C_D = \frac{a_{schiller}}{Re_P}\left(1 + 0.15 Re_P^{0.687}\right) \tag{8}$$

Therefore, the drag coefficient of the coal and char particles can be obtained by applying a spherical approximation to the non-spherical particles and experimentally determining the coefficient a in the expressions above.

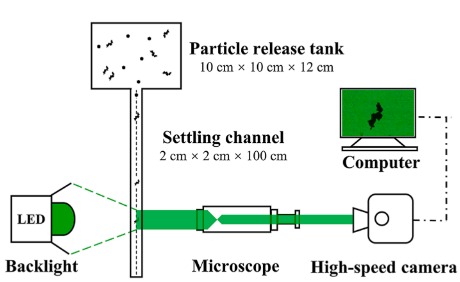

Fig. 1. Schematic of the particle settling experimental setup.

2.2. Experimental setup

The schematic of the experimental setup is shown in Fig. 1, which comprises two main subsystems: a particle settling system and an optical measurement system. A mass of coal and char particles are initially released from a particle release tank (10 cm × 10 cm × 12 cm), a portion of these particles enters the settling channel (2 cm × 2 cm × 100 cm). The settling channel has a cross section of 2 cm × 2 cm, which is much larger than the particle size. A gentle airflow was used to disturb the particles in the particle release tank, resulting in an extremely low particle concentration entering the channel. Thus, the probability of overlap between particles is very low, thereby reducing the likelihood of particle projection overlap. The entire release assembly is constructed from transparent PVC to facilitate visual observation. The settling channel is designed with sufficient width to ensure that the wall effects are negligible for particles with diameter of 200 μm and smaller. Furthermore, the channel length is adequate to allow particles to achieve fully developed, stable settling motion. The particle settling process was recorded using a high-speed camera (UX100, Photron) coupled with a microscope. Particle settling velocities at various vertical heights were calculated via image analysis to determine whether the particles had reached a fully developed and stable settling state. This information was subsequently used as the criterion for determining the final imaging position. To obtain high-contrast images, a high-power green LED backlight was employed to illuminate the particles against the background. The focal plane of the microscope was aligned with the center line of settling channel to ensure that the recorded particles were within the region unaffected by wall effects, thereby capturing their free-settling behavior. Imaging was performed at a fixed magnification of 20×. Under such magnification, the microscope has a very shallow depth of field, such that only particles within the same focal plane are clearly imaged. This avoids overlapping images of particles from different focal planes, which prevents their misidentification as a single particle. The high-speed camera was operated at 1000 frames per second with an exposure time of 1 – 3 μs and a resolution of 1280 × 1024 pixels. All experiments were conducted under controlled ambient conditions: temperature was maintained at 25 °C and relative humidity at 10%, corresponding to an air viscosity of 1.846×10^{-5} Pa s and an air density of 1.184 kg m^{-3}. The temperature was held constant to maintain the physical properties of air, such as density and viscosity, thereby minimizing measurement errors caused by environmental fluctuations and ensuring the reproducibility of the experimental data. The relative humidity was controlled to avoid the interference of liquid bridges between particles on the drag characteristics, which could occur when moisture level is high.

The coal used in the experiments is low-rank coal obtained from the Northern Shaanxi region of China, one of the most important low-rank coal producing areas in the country. The corresponding char was produced via pyrolysis of this coal, ensuring that the samples are representative of industrial practice. The densities of the coal and char particles were measured by the gas pycnometry method according to ISO 12154, giving values of 896 and 1180 kg m^{-3}, respectively. Particle size distribution (PSD) describes the relative abundance of particles across different size classes and is commonly characterized by

Table 2
Particle size distribution data of coal and char particles used in experiments.

Particle type	D_{10}	D_{25}	D_{50}	D_{75}	D_{90}	D_{97}	Span
	μm	μm	μm	μm	μm	μm	-
Char particles	6.25	14.83	34.39	67.98	110.55	153.97	3.033
Coal particles	19.27	49.95	114.55	207.14	331.24	495.98	2.723

parameters such as D_{10}, D_{50}, D_{90}, and Span, where D_{10}, D_{50}, and D_{90} represent the particle diameters at cumulative percentages of 10%, 50%, and 90%, respectively, and Span is defined as $(D_{90}-D_{10})/D_{50}$, reflecting the width of the distribution. The PSDs of the coal and char particles were determined using a laser diffraction particle size analyzer (LS-909, OMEC) in accordance with ISO 13320, and the results are shown in Table 2. The size distributions of both particles approximately follow normal distributions. The median particle diameter (D_{50}) of coal is 114.55 μm, while that of char is 34.39 μm. The Span value, which reflects the width of the size distribution, is 2.723 for coal particles and 3.033 for char particles. This indicates that after coal pyrolysis, the particle size becomes smaller overall, while the width of the size distribution correspondingly broadens.

The morphology of a large number of individual particles and aggregates captured during the experiments was analyzed using ImageJ software in accordance with ISO 13322-2:2020. The results show that for coal individual particles, the aspect ratio ranges from 1.145 to 1.534 with an average of 1.336; for coal aggregates, it ranges from 1.807 to 2.693 with an average of 2.145; for char individual particles, it ranges from 1.389 to 1.624 with an average of 1.564; and for char aggregates, it ranges from 2.215 to 2.974 with an average of 2.507. These data indicate that for both materials, the average aspect ratio of aggregates is higher than that of single particles, and the average aspect ratios of char, both individual particles and aggregates, are higher than those of coal.

2.3. Data processing

During data processing, we screened and analyzed a sequence of time-series images to ensure that the selected particle images remained stable and did not separate throughout the settling process. Since two distinct particles do not follow identical settling paths, if their projections overlap in the imaging plane, they will inevitably diverge over time. Any data exhibiting such overlap were therefore discarded. Based on these screened data, particle settling behavior was analyzed using a digital image processing algorithm to determine key parameters including particle size, projected area, and terminal velocity. Particle positions at different times were superimposed into a single composite image. Uniform displacement over equal time intervals confirms that the particles had reached steady-state settling. We differentiate individual particles and aggregates through a three-level identification process: (1) preliminary screening based on equivalent particle diameter and aspect ratio; (2) morphological identification based on light transmission characteristics in backlight images; (3) final verification based on settling velocity characteristics. This three-step process ensures the accurate differentiation between individual particles and aggregates. Fig. 2(a) and (b) depict the fully developed settling of an individual particle and a particle aggregate respectively. Then, the images were binarized to obtain the two-dimensional projection of the particles. For micron-sized particles, it is extremely challenging to capture the windward projected area via a microscope without interfering with the motion of free-settling particles. In this experiment, the high-speed camera and microscope system were arranged horizontally, with the shooting direction perpendicular to the vertical settling direction of the particles, and the imaging plane parallel to the particle settling direction. The equivalent particle diameter was calculated based on the images captured by the high-speed camera. Therefore, the two-dimensional projected area obtained in this work corresponds to the projected area perpendicular to the particle settling direction. For irregular particles, the equivalent particle diameter, d_{eq}, was defined based on the projected area as follows:

$$d_{eq}=\sqrt{\frac{4A_{sh}}{\pi}} \tag{9}$$

where A_{sh} is the two-dimensional projection area of the particle on the imaging plane.

The stable terminal settling velocity of the individual particle or the particle aggregate, U_t can be calculated from the image:

$$U_t=\frac{fL(\Delta n)}{n} \tag{10}$$

Where f is the frame rate of the high-speed camera and $L(\Delta n)$ represents the settling displacement of the particle over a duration of n frames.

The calculation formula for the mean relative error of the fitted correlations is given below:

$$\text{Mean Relative Error}=\frac{1}{n}\sum_{i=1}^{n}\left(\frac{\text{Measured}_i-\text{Predicted}_i}{\text{Measured}_i}\times 100\%\right) \tag{11}$$

2.4. Experimental platform validation

To validate the reliability of the experimental method, free-settling experiments were first conducted using water microdroplets, and the obtained C_D were compared against predictions from Stokes and Schiller drag correlations. The microdroplets were generated by atomizing deionized water with a high-pressure spray bottle. Owing to surface tension, the resulting droplets exhibited high sphericity, as shown in Fig. 3(a). Fig. 3(b) presents a comparison between the drag coefficients of microdroplets obtained using the method described in this work and predictions from Stokes and Schiller correlations across a range of particle Reynolds numbers. The results indicate that for particle Reynolds numbers less than 0.26, the measured drag coefficients agree well with predictions from both models. For particle Reynolds numbers greater than 0.26, the calculated drag coefficients align closely with the Schiller model. These findings are consistent with observations reported in previous studies (Ma et al., 2022). The favorable agreement validates the accuracy of the experimental methodology employed in this study.

3. Results and discussion

The measured terminal settling velocities of the individual particles and the particle aggregates with various equivalent particle diameters from 5 to 200 μm are shown in Fig. 4, where the terminal settling velocities changed between 2×10^{-3} and 6×10^{-1} m s^{-1}. The settling velocity of both coal and char particles exhibits a power-law dependence on the equivalent particle diameter. A comparison between the two materials shows that, for particles with the same equivalent particle diameter, the settling velocity of char particles is substantially higher than that of coal particles, typically by a factor of about three. This difference can likely be attributed to the higher density of char compared to coal. Therefore, when the projected windward area is the same, char particles reach steady settling more rapidly and attain a greater terminal settling velocity.

Unlike microdroplets, coal and char particles display a wide distribution of terminal settling velocities due to their highly irregular shapes and rough surfaces. As shown in Fig. 5, char particles vary considerably in morphology, including nearly spherical, elongated, and highly irregular forms. Even among particles with similar shapes, their steady-

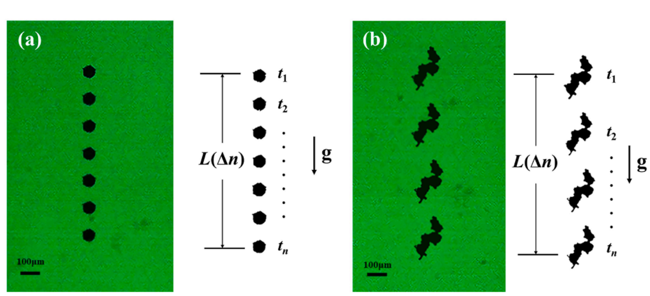

Fig. 2. Stabilized settling process diagram of: (a) single particle and; (b) particle aggregate.

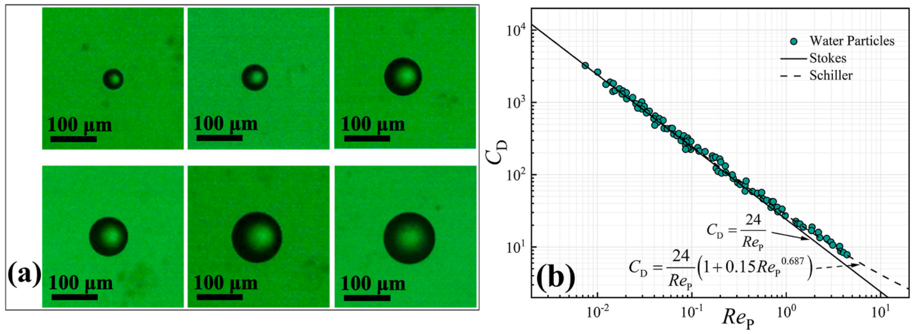

Fig. 3. Experimental validation using microdroplets: (a) experimentally captured images of microdroplets; (b) comparison of the measured drag coefficient (C_D) with predictions from Stokes and Schiller correlations.

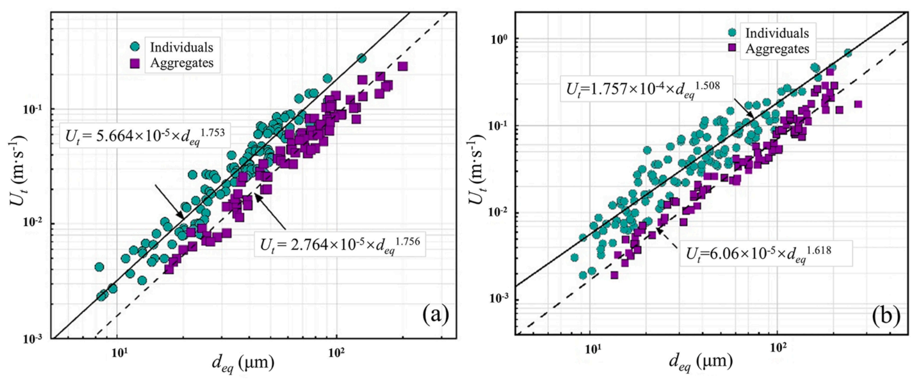

Fig. 4. The relationship between the terminal settling velocity and the equivalent particle diameter for (a) individual coal particles and coal aggregates; (b) individual char particles and char aggregates. The equivalent particle diameter is from 5 to 200 μm.

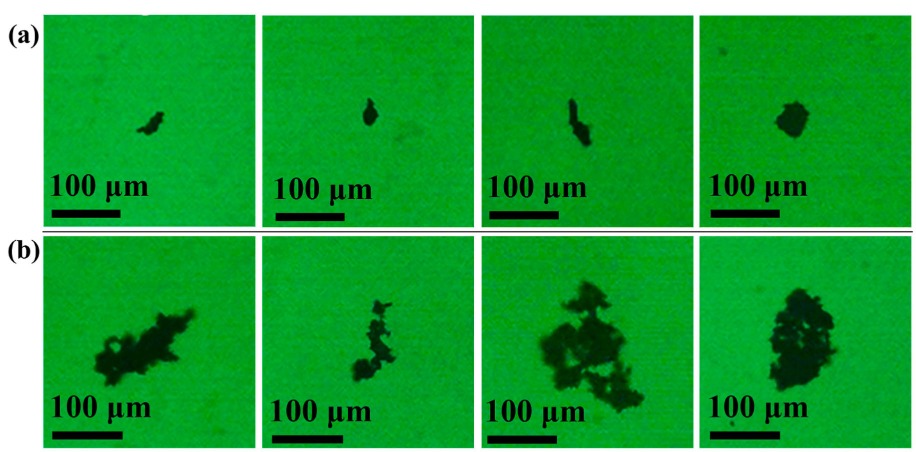

Fig. 5. Captured images of typical char particles in the experiment: (a) individuals; (b) aggregates.

state settling behavior differs significantly. For instance, when elongated particles settle with their major axis aligned with the direction of motion, they present a smaller windward area, resulting in a lower drag coefficient and hence a higher settling velocity. Conversely, if the major axis is inclined or perpendicular to the settling direction, the windward area increases substantially, leading to a lower settling velocity. This effect contributes to notable variation in the terminal velocities of particles with similar sizes. Moreover, individual particles generally settle faster than particle aggregates. It is because particle aggregates exhibit elevated porosity, which amplifies fluid entrainment and induces complex interstitial flows during settling. This flow complexity enhances both form drag and skin friction on particle aggregates, collectively increasing hydrodynamic resistance and reducing terminal settling velocity.

Based on experimental data, the terminal settling velocity formulas were fitted for individual coal particles, coal particle aggregates, individual char particles and char particle aggregates, with equivalent diameters ranging from 5 to 200 μm.

Individual coal particles:

$$U_t = 5.664 \times 10^{-5} \times d_{eq}{}^{1.753} \tag{12}$$

Coal particle aggregates:

$$U_t = 2.764 \times 10^{-5} \times d_{eq}{}^{1.756} \tag{13}$$

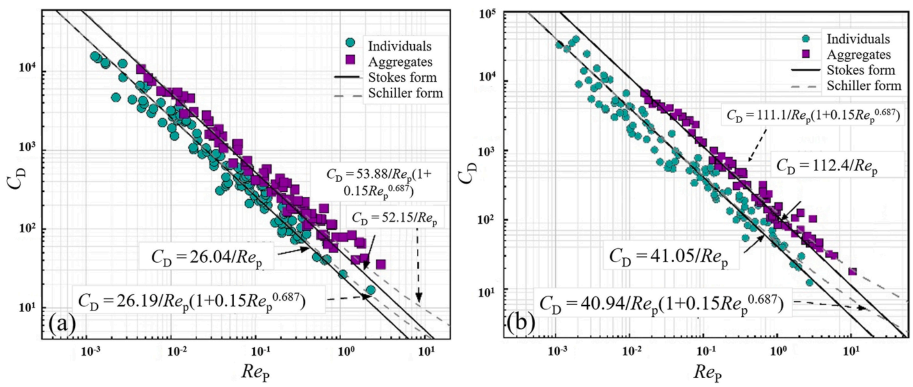

Fig. 6. The relationship between drag coefficient and particle Reynolds number for (a) individual coal particles and coal aggregates; (b) individual char particles and char aggregates. The equivalent particle diameter is from 5 to 200 μm.

Individual char particles:

$$U_t = 1.757 \times 10^{-4} \times {d_{eq}}^{1.508} \tag{14}$$

Char particle aggregates:

$$U_t = 6.06 \times 10^{-5} \times {d_{eq}}^{1.618} \tag{15}$$

In these formulas, U_t is the terminal settling velocity, in m s^{-1}; d_{eq} is the equivalent particle diameter, in μm. The mean relative errors of the above fitted correlations are 23.39% for individual coal particles, 20.35% for coal aggregates, 38.25% for individual char particles, and 28.35% for char aggregates, respectively.

Based on the terminal settling velocities and equivalent particle diameters obtained from the aforementioned experiments, and by analogy with the Stokes and Schiller expressions, the drag coefficients for individual coal particles, individual char particles, coal aggregates, and char aggregates can be further derived. The drag coefficients corresponding to different particle Reynolds numbers are presented in Fig. 6. Under the experimental conditions investigated in this study, the particle Reynolds number ranged from 10^{-3} to 10^1, while the corresponding drag coefficient C_D varied from 10^1 to 10^5. An inverse correlation was observed between C_D and the particle Reynolds number: as the particle Reynolds number increased, the drag coefficient decreased for both individual particles and their aggregates. Taking pulverized coal as an example, when the particle Reynolds number increased from 10^{-3} to 10^1, the drag coefficient of individual particles decreased from 1.57×10^4 to 1.67×10^1, and that of coal aggregates decreased from 1.1×10^4 to 3.58×10^1. Furthermore, as shown in the figure, when the particle Reynolds number is below 3×10^{-1}, the variation of C_D exhibits a nearly linear trend in logarithmic coordinates. However, for the particle Reynolds number exceeding 3×10^{-1}, the drag coefficient deviates significantly from this linear behavior. Notably, under the same equivalent particle diameter conditions, both individual char particles and char aggregates exhibit higher drag coefficients compared to their coal counterparts. For instance, at the same particle Reynolds number, the drag coefficient of an individual char particle is approximately 1.58 times that of an individual coal particle, while the drag coefficient of a char aggregate is about 2.06 times greater than that of a coal aggregate. This indicates distinct dynamic characteristics between char and coal particles.

Based on the drag coefficients obtained across different particle Reynolds numbers in this study, empirical correlations can be developed for the drag coefficients of individual coal particles, coal aggregates, individual char particles, and char aggregates within the diameter range of 5 to 200 μm. The theoretical basis for the correlation development is established on the classical Stokes and Schiller formulations: Stokes derived the analytical solution of the drag coefficient for standard spherical particles in the creeping flow regime ($Re_p < 1$) as $C_D = 24/Re_p$, where the coefficient 24 is a theoretical constant with a clear physical basis, calculated from the windward area of spherical particles. The Schiller correlation extends the applicable range of the Stokes formulation to the laminar transition regime while retaining the coefficient 24, with the exponent 0.687 being a classic empirical parameter for range extension. In this work, we modified the coefficient 24 to adapt the correlation to highly irregular non-spherical char and coal particles, while retaining the classical empirical exponent 0.687. This treatment is adopted because the applicable particle Reynolds number range of the correlation derived in this study does not exceed that of the original Schiller correlation, thus no modification to the Re_p-dependent correction term is required. Within the framework of the Schiller formulation, the fitted coefficients a for individual particles are determined as 26.19 ± 3.4 for coal and 40.94 ± 3.2 for char, which closely approximate the corresponding values of 26.04 ± 3.5 for coal and 41.05 ± 3.2 for char derived from the Stokes model. For particle aggregates, the coefficients under the Schiller and Stokes formulations are 53.88 ± 4.2 and 52.15 ± 4.8 for coal, and 111.1 ± 4.2 and 112.4 ± 4.3 for char, respectively. The revised drag coefficient expression is presented below:

Individual coal particles:

$$C_{D,Stokes} = \frac{26.04}{Re_p} \tag{16}$$

$$C_{D,Schiller} = \frac{26.19}{Re_p}\left(1 + 0.15{Re_p}^{0.687}\right) \tag{17}$$

Coal particle aggregates:

$$C_{D,Stokes} = \frac{52.15}{Re_p} \tag{18}$$

$$C_{D,Schiller} = \frac{53.88}{Re_p}\left(1 + 0.15{Re_p}^{0.687}\right) \tag{19}$$

Individual char particles:

$$C_{D,Stokes} = \frac{41.05}{Re_p} \tag{20}$$

$$C_{D,Schiller} = \frac{40.94}{Re_p}\left(1 + 0.15{Re_p}^{0.687}\right) \tag{21}$$

Char particle aggregates:

$$C_{D,Stokes} = \frac{112.4}{Re_p} \tag{22}$$

$$C_{D,Schiller} = \frac{111.1}{Re_p}\left(1 + 0.15{Re_p}^{0.687}\right) \tag{23}$$

Under the Stokes formulation, the mean relative errors are 23.70%

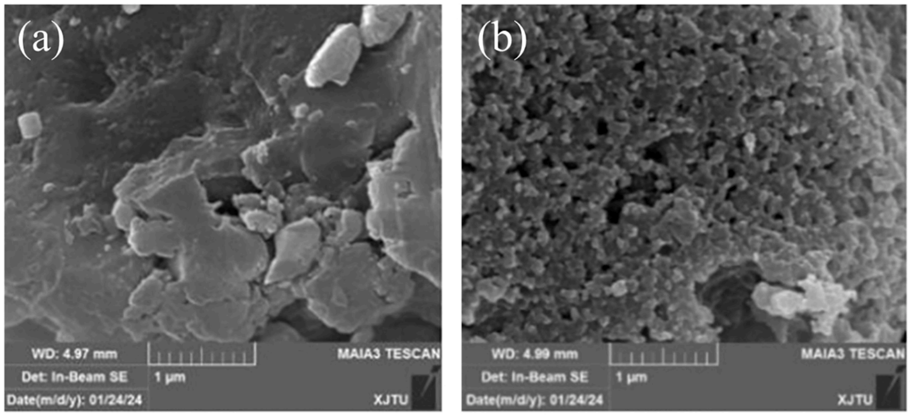

Fig. 7. The SEM images of the coal and char microparticles: (a) coal particle; (b) char particle.

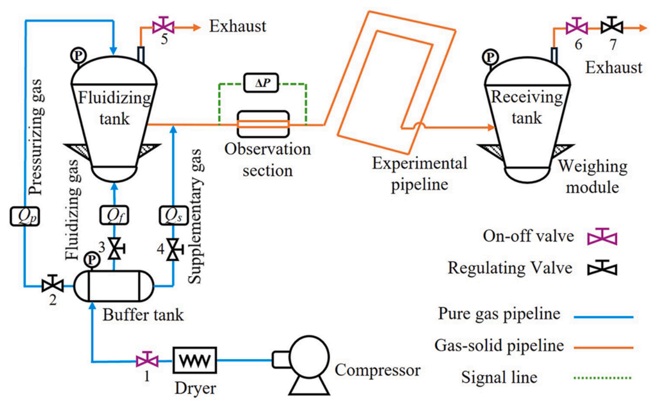

Fig. 8. Schematic of the pneumatic conveying experimental setup (numbers 1-7 represent the valves in the system).

for individual coal particles, 32.08% for coal aggregates, 32.09% for individual char particles, and 27.24% for char aggregates, respectively. Under the Schiller formulation, the mean relative errors are 22.77% for individual coal particles, 25.02% for coal aggregates, 20.83% for individual char particles, and 21.24% for char aggregates, respectively.

To further investigate the underlying causes of the distinct settling dynamics between char particles and coal particles, scanning electron microscopy (SEM) was employed using an ultra-high resolution field emission scanning electron microscope (MAIA3, TESCAN), following ISO 22493 to capture their microscopic morphologies, as shown in Fig. 7. The results indicate that, compared with coal powder, char powder exhibits a more porous structure and a rougher surface morphology. This is attributed to the fact that char powder is a product of high-temperature pyrolysis of coal. During the pyrolysis process, the release of volatile gases, tar, and other substances generates numerous cavities on the particle surface, leading to a more porous internal structure and a rougher surface texture compared to its coal counterpart. Based on fluid dynamics theory, it can be inferred that such a porous structure and rougher surface morphology enhance the interaction between char particles and the surrounding air during settling. This intensified interaction alters the boundary layer state, modifies the structure and pressure distribution of the wake, and increases energy dissipation, consequently resulting in a higher drag coefficient for char compared to coal powder.

To validate the drag coefficient model for char powder proposed in this study, a dedicated pneumatic conveying experimental system was constructed. The schematic of the experimental setup is presented in

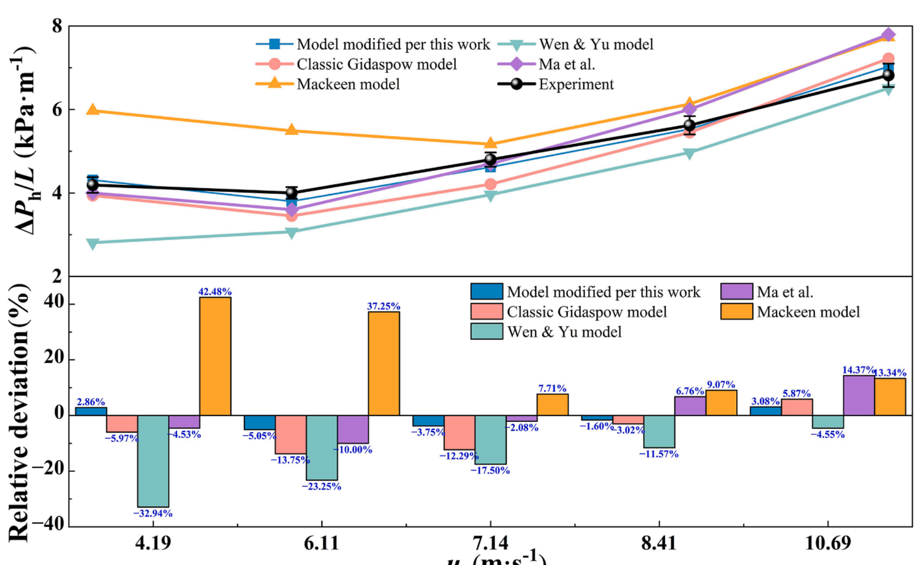

Fig. 9. Comparison between experimental data and model predictions for the pressure drop per unit length in the horizontal pipe: simulated values versus measured data and the relative deviations of models.

Fig. 8. The pressure drop per unit length was measured experimentally. The results were then compared with simulation results obtained using the drag model developed in this work and other widely used drag models.

The gas-solid two-phase flow model for the pneumatic conveying of char powder is detailed in the supplementary data. The characteristic particle size is a core input parameter for this model, the windward projected area of individual irregular non-spherical particles varies with particle orientation during gas flow, which complicates the definition of equivalent particle diameter. However, in the pneumatic conveying process, the variation in projected area of bulk particles exhibits a stable statistical regularity. Therefore, it is more rational to adopt the statistically averaged equivalent diameter of bulk particles, rather than the diameter of a single particle, as the characteristic particle size in our numerical simulations. In the validation numerical simulations, all char particles are treated as individual particles in the model calculation, as the vast majority of char powder particles exist in the form of individual particles under the conveying conditions. This comparison is illustrated in Fig. 9, where u_g denotes gas velocity. The pressure drop in the horizontal pipe exhibits a trend of first decreasing and then increasing with the rise of superficial gas velocity, and reaches the minimum value at the superficial gas velocity of 6.11 m s^{-1}. This phenomenon is directly related to the flow state of particles in pneumatic conveying. At low superficial gas velocity, the frictional pressure drop from inter-particle friction dominates the total pressure drop, which decreases with the thinning of the particle deposited layer as gas velocity increases. As gas velocity further rises, the pressure drop required to maintain particle suspension becomes the dominant component, leading to an increase in the total pressure drop.

The pressure drop of pneumatic conveying is a macroscopic result reflecting the energy transfer and dissipation between gas and solid phases during the flow process. The prediction performance of the model for pressure drop directly reflects the accuracy of the model in describing the actual physical process. Therefore, the conveying pressure drop is adopted as the core indicator for model validation and comparison in this work. Comparisons are conducted between five drag models to further validate the performance of the proposed model: the modified drag model developed in this study, the classical Gidaspow model (Gidaspow et al., 2004), the Wen & Yu model (Wen & Yu, 1966), the Mckeen model (McKeen & Pugsley, 2003), and a non-spherical drag model modified based on the correlation for irregular sand particles proposed by Ma et al. The pressure drop predictions of all models are compared with experimental data over the apparent gas velocity range of 4.19–10.69 m s^{-1}. The maximum pressure drop prediction errors are 5.05% (this study), 13.75% (Gidaspow), 32.94% (Wen & Yu), 42.48% (Mckeen) and 14.37% (Ma et al.), respectively. Comparative analysis reveals that the drag model developed in this work achieves better agreement with experimental data compared to existing models. Specifically, it exhibits a maximum pressure drop prediction error of 5.05%, representing a significant improvement over both widely used drag models and the non-spherical drag model modified by Ma's correction (Ma et al., 2022). These findings confirm the accuracy of the proposed char powder drag model, which offers a more reliable numerical framework for char powder pneumatic conveying simulations and enables more effective optimization of industrial-scale conveying systems.

4. Conclusion

This study establishes, for the first time, a quantitative drag coefficient correlation for non-spherical char powder particles as a function of Reynolds number, which incorporates the effect of particle morphology during the fitting process. The drag coefficient of char is significantly higher (1.58 - 2.06 times) than that of its parent coal under identical conditions. These results directly address the lack of reliable drag coefficient data for char particles. The higher drag is mechanistically linked to the porous and rougher surface morphology of char, originating from volatile release during pyrolysis, which intensifies fluid-particle interaction and energy dissipation in the settling process. Our char-specific model, validated against both settling and pneumatic conveying experiments, provides a physics-based improvement over the classical Gidaspow model, reducing prediction deviations by 63.27%.

In future research, the operating conditions can be further expanded to improve the applicability of the findings in industrial applications. For instance, high-pressure conditions are commonly adopted in industrial pneumatic conveying, therefore, it is suggested that subsequent investigations be carried out under realistic conveying pressures, to reveal the settling characteristics of particles in high-pressure environments. In addition, another research objective is to investigate the factors influencing particle aggregation. For example, experiments could be conducted under varying relative humidity levels to explore how ambient humidity affects particle aggregation behavior and the resulting drag characteristics.

CRediT authorship contribution statement

Wenyu Tu: Writing – original draft. **Peilin Tian:** Visualization, Validation. **Liang-Liang Fan:** Writing – review & editing. **Liang Zhao:** Supervision, Funding acquisition.

Declaration of competing interest

The authors declare that they have no known competing financial interests or personal relationships that could have appeared to influence the work reported in this paper.

Acknowledgment

This work was supported by Shaanxi Provincial Natural Science Foundation Research Program Shaanxi Coal Joint Funding (No. 2021JLM-21).

Appendix A. Supplementary data

Supplementary data to this article can be found online at https://doi.org/10.1016/j.partic.2026.05.022.

References

Bagheri, G., & Bonadonna, C. (2016). On the drag of freely falling non-spherical particles. *Powder Technology, 301*, 526–544.
Bagheri, G., & Bonadonna, C. (2019). Comment on "A New One-Equation Model of Fluid Drag for Irregularly Shaped Particles Valid Over a Wide Range of Reynolds Number" by F. Dioguardi et al. *Journal of Geophysical Research: Solid Earth, 124*(10), 10261–10264.
Brown, P. P., & Lawler, D. F. (2003). Sphere drag and settling velocity revisited. *Journal of Environmental Engineering, 129*(3), 222–231.
Cai, J., Xu, J., You, M., Liang, C., Liu, D., Ma, J., & Chen, X. (2023). Flow characteristics and pattern transition of different pipe diameters in pneumatic conveying for gasifier. *Chemical Engineering Research and Design, 189*, 282–295.
Cheng, N.-S. (2009). Comparison of formulas for drag coefficient and settling velocity of spherical particles. *Powder Technology, 189*(3), 395–398.
Clift, R., & Gauvin, W. H. (1971). Motion of entrained particles in gas streams. *Canadian Journal of Chemical Engineering, 49*(4), 439–448.
Dioguardi, F., & Mele, D. (2015). A new shape dependent drag correlation formula for non-spherical rough particles. Experiments and results. *Powder Technology, 277*, 222–230.
Dioguardi, F., Mele, D., & Dellino, P. (2018). A new one-equation model of fluid drag for irregularly shaped particles valid over a wide range of reynolds number. *Journal of Geophysical Research: Solid Earth, 123*(1), 144–156.
Fang, Z., Zhang, Y., Zhao, S., Li, X., Wu, X., & Sun, L. (2021). An experimental investigation on the settling velocity and drag coefficient of micrometer-sized natural, IG-110, NG-CT-10 and A3-3 graphite particles. *Journal of Aerosol Science, 155*, Article 105774.
Ganser, G. H. (1993). A rational approach to drag prediction of spherical and nonspherical particles. *Powder Technology, 77*(2), 143–152.
Gidaspow, D., Jung, J., & Singh, R. K. (2004). Hydrodynamics of fluidization using kinetic theory: An emerging paradigm: 2002 Flour-Daniel lecture. In *Powder technology, selected papers from the 3b Panel at the 2002 AIChE meeting in Indianapolis* (Vol. 148, pp. 123–141), 2.

Goossens, W. R. A. (2019). Review of the empirical correlations for the drag coefficient of rigid spheres. *Powder Technology, 352*, 350–359.

Haider, A., & Levenspiel, O. (1989). Drag coefficient and terminal velocity of spherical and nonspherical particles. *Powder Technology, 58*(1), 63–70.

Hölzer, A., & Sommerfeld, M. (2008). New simple correlation formula for the drag coefficient of non-spherical particles. *Powder Technology, 184*(3), 361–365.

Hussain, M., & Munshi, B. (2024). An experimental investigation on the settling of disk particles in annular region: Wall effect and drag coefficient. *Particulate Science & Technology, 42*(5), 859–873.

Li, H., & Tomita, Y. (2000). A numerical simulation of swirling flow pneumatic conveying in a horizontal pipeline. *Particulate Science and Technology, 18*(4), 275–291.

Liu, Z., Rao, Q., Yi, W., & Huang, W. (2024). A modified drag coefficient model for calculating the terminal settling velocity and horizontal diffusion distance of irregular plume particles in deep-sea mining. *Environmental Science and Pollution Research, 31*(23), 33848–33866.

Loth, E. (2008). Drag of non-spherical solid particles of regular and irregular shape. *Powder Technology, 182*(3), 342–353.

Ma, X., Ji, G., Li, Z., & Ju, G. (2022). An improved model for predicting the drag coefficient and terminal settling velocity of natural sands in newtonian fluid. *Processes, 10*(8).

Ma, A., Williams, K. C., Zhou, J., & Jones, M. G. (2012). Experimental and numerical research on pressure gradient of a pneumatic conveying pipeline of flyash. In *2012 second international conference on intelligent System design and engineering application* (pp. 1247–1250).

Marchildon, E. K., Clamen, A., & Gauvin, W. H. (1964). Drag and oscillatory motion of freely falling cylindrical particles. *Canadian Journal of Chemical Engineering, 42*(4), 178–182.

Marshall, J. S., & Li, S. (2014). Fluid forces on particles. In *Adhesive particle flow: A discrete-element approach* (pp. 130–181). Cambridge University Press.

McKeen, T., & Pugsley, T. (2003). Simulation and experimental validation of a freely bubbling bed of FCC catalyst. *Powder Technology, 129*(1–3), 139–152.

Miao, Z., Kuang, S., Zughbi, H., & Yu, A. (2020). Numerical simulation of dense-phase pneumatic transport of powder in horizontal pipes. *Powder Technology, 361*, 62–73.

Pu, W., Zhao, C., Xiong, Y., Liang, C., Chen, X., Lu, P., & Fan, C. (2010). Numerical simulation on dense phase pneumatic conveying of pulverized coal in horizontal pipe at high pressure. *Chemical Engineering Science, 65*(8), 2500–2512.

Schiller, L., & Naumann, A. (1933). Uber die Grundlegenden Berechnungen bei der Schwerkraftaufbereitung. *Z. Vereines Deutscher Inge., 77*, 318–321.

Song, Z., Wu, T., Xu, F., & Li, R. (2008). A simple formula for predicting settling velocity of sediment particles. *Water Science and Engineering, 1*(1), 37–43.

Song, X., Xu, Z., Li, G., Pang, Z., & Zhu, Z. (2017). A new model for predicting drag coefficient and settling velocity of spherical and non-spherical particle in Newtonian fluid. *Powder Technology, 321*, 242–250.

Stokes, G. G. (2009). *Mathematical and physical papers* (1st ed.). Cambridge University Press.

Tang, Q., Zhang, J., Zhong, J., Li, K., Gao, B., Wang, Z., Xu, R., Wang, G., & Liu, Z. (2017). Utilization of semi-coke in iron making technologies in China. *Metallurgical Research & Technology, 114*(4), Article 4.

Wang, Y., Zhou, L., Wu, Y., & Yang, Q. (2018). New simple correlation formula for the drag coefficient of calcareous sand particles of highly irregular shape. *Powder Technology, 326*, 379–392.

Wen, C. Y., & Yu, Y. H. (1966). Mechanics of fluidization. *Fluid Particle Technology, Chem. Eng. Progress. Symposium Series, 62*, 100–111.

Xiao, K., Liu, X., Hu, H., Wen, Z., & Lou, G. (2024). Heat and mass transfer analysis of coal coking process in the coking chamber. *International Journal of Coal Preparation and Utilization, 44*(10), 1732–1747.

Xu, Z., Shen, K., Zhang, K., Guo, N., & Li, Z. (2024). A new model for predicting drag coefficient and settling velocity of coarse mineral particles in newtonian fluid. *Minerals, 14*(2), Article 2.

Zhu, Y., Li, K., Wang, Q., Cen, J., Fang, M., & Luo, Z. (2022). Low-rank coal pyrolysis polygeneration technology with semi-coke heat carrier based on the dual-fluidized bed to co-produce electricity, oil and chemical products: Process simulation and techno-economic evaluation. *Fuel Processing Technology, 230*, Article 107217.